Extreme Mechanics Letters 68 (2024) 102134

Contents lists available at ScienceDirect

Extreme Mechanics Letters

journal homepage: www.elsevier.com/locate/eml

Capsizing due to friction-induced twist in the failure of stopper knots

Paul Johanns, Pedro M. Reis *

Flexible Structures Laboratory, Institute of Mechanical Engineering, École Polytechnique Fédérale de Lausanne (EPFL), Lausanne, Switzerland

ARTICLE INFO

Keywords:
Mechanics of knots
Stopper knots
Capsizing
Experiments
Finite element modeling

ABSTRACT

We investigate the failure mechanism of stopper knots, with a particular focus on the figure-8 knot as a representative example. Stopper knots are widely used in climbing, sailing, racket stringing, and sewing to maintain tension in ropes, strings, or threads while preventing them from passing through an orifice. Combining high-precision model experiments and Finite Element Analyses, we systematically explore the influence of frictional interactions and their role in the build-up of mechanical twist. Our findings reveal that the failure of stopper knots via capsizing, which involves configurational alterations of the filament, is primarily due to friction-induced twisting when loading the knot against a restraining plate containing a clearance hole. Our study offers a comprehensive understanding of the mechanical behavior of stopper knots under diverse loading conditions, thereby providing crucial insights for their reliable application across various domains.

1. Introduction

In functional knots, topology, geometry, and mechanics interact closely to determine performance, which is especially important in applications where stability is crucial for their operational integrity and safety. Catastrophic consequences may ensue from failure modes such as fracture or unraveling; for instance, when a *hitch* used for boat mooring unravels [1], a *bend* joining two ropes in rock climbing unties [2], or a *binding knot* in surgical suturing slips open [3,4]. Knot stability has been previously studied for common binding knots and bends [5–7]. However, unlike these 2-tangle configurations, 1-tangle knots, also known as "stopper knots", typically serve a distinct functional role. Specifically, these knots are designed to resist unraveling when a knotted filament (*e.g.*, a rope or string) is tensioned by pulling it through an orifice in a stopper object (*e.g.*, climber's belay device or a tennis racket frame).

The ubiquitous stopper knots are often included in knot manuals [8–11]. In sewing, they secure the thread, preventing withdrawal through the needle's eye. In climbing, a stopper knot prevents the rope from slipping through the belay device. In sailing, bulky knots in the 'footrope' aid sailors in standing while manipulating sails. During the stringing of tennis rackets, half-hitches at the string extremities anchor it to the frame, stabilizing tension. Despite their widespread use, existing literature on stopper knots focuses on the potential for jamming and knot bulkiness as primary performance metrics [8,10]. For instance, the overhand knot is identified as susceptible to jamming and can induce rope damage [8]. While the Stevedore and Ashley's stopper knots are regarded as superior [10], they see less frequent application due to their complex topologies. Notably, the figure-8 and double-overhand knots (4_1 and 5_1, respectively, using Alexander-Briggs notation [12]) are among the most common stopper knots. More recently, Tong et al. [13], studied the mechanical response of the fisherman's knot, comprising two filament strands, each connected to the other by two trefoil overhand knots at their extremities; each knot can be regarded as a stopper knot to the other strand. The authors performed a comprehensive investigation of different modes of failure (*e.g.*, sliding-then-fracture, stretching-then-fracture, and untangling) of this knotted system.

Capsizing is another frequently encountered yet often undesirable phenomenon in physical knots, involving the reconfiguration of the knot's geometry due to external loads while preserving its topology [8,9]. Intentional rearrangement of rod segments may be advantageous for dislodging jammed knots; however, inadvertent capsizing presents a significant risk, particularly when the external load can no longer be sustained as the knot slips through the filament's extremity. Despite the general awareness of capsizing among practitioners, especially sailors, and climbers, the underlying kinematics and mechanics of this behavior remain largely unexplored in the literature.

Here, we study the stability of stopper knots via precision experiments and Finite Element Method (FEM) simulations. An elastic rod is threaded through the clearance hole of a stopper plate, and a figure-8 knot is tied at the rod's lower end. Upon pulling the rod's upper end, the knot is restrained against the plate, causing a significant tension reduction between the pulling and the lower ends, the latter set by a dead weight (Fig. 1**a** and S.I. Movie). Upon further load increase,

* Corresponding author.
E-mail address: pedro.reis@epfl.ch (P.M. Reis).

https://doi.org/10.1016/j.eml.2024.102134
Received 14 November 2023; Received in revised form 5 February 2024; Accepted 7 February 2024
Available online 12 February 2024

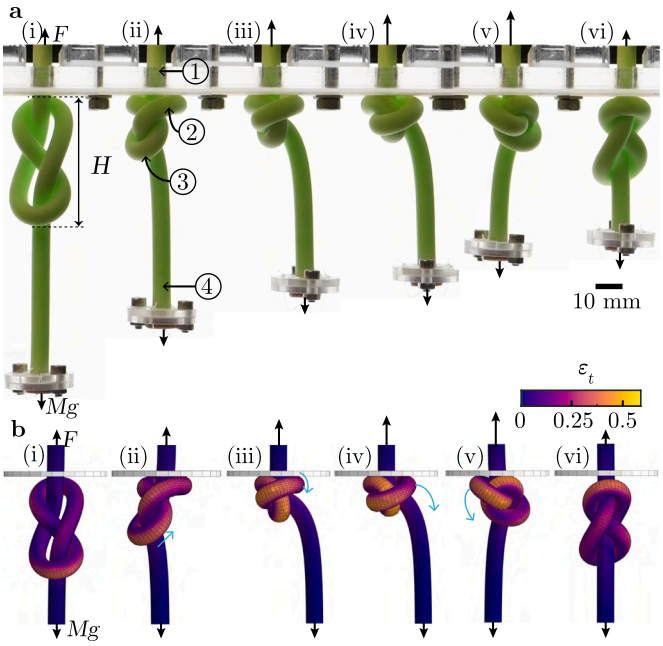

Fig. 1. Model system for a figure-8 stopper knot. **a, b**, Sequence of experimental (**a**) and FEM (**b**) snapshots of a figure-8 knot loaded against a stopper plate. The initial knot size is H/D=6.6±0.1. The labels on the rod in (**a**) designate the pulled end (1), the upper loop (2), the lower loop (3), and the free end (4). The latter is loaded by a dead weight, Mg. In (**b**), for visualization, the color map displays the maximum principal true strain in the rod at the arc-length s. Each configuration, from (i) to (vi), corresponds to identical loading levels in experiments and FEM. See S.M. Video.

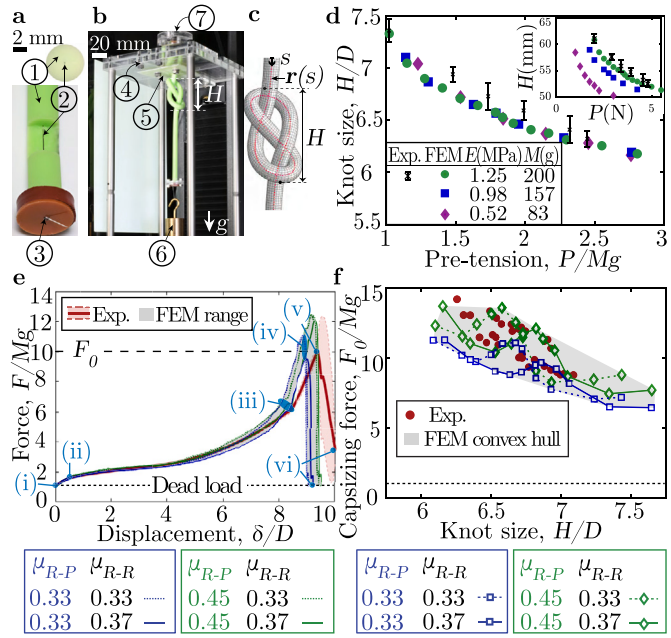

Fig. 2. Fabrication and testing of figure-8 stopper knots. **a**, Composite rod with VPS matrix (1) and a NiTi-wire core (2); top: cross-section, bottom: NiTi wire with overhand knots (3) at its ends. A semi-cylinder portion has been cut out to visualize the wire. **b**, Apparatus featuring a stopper plate (4) coated by a VPS film (5), and a dead load, Mg (6). The upper end of the rod is loaded by a UTM (7). **c**, Configuration of a FEM-simulated knot, showing the mesh and the fiber reinforcement (dashed centerline at $\boldsymbol{r}(s)$). **d**, Normalized knot size, H/D, before testing, vs. the applied pre-tension, $P/(Mg)$; the inset: dimensional plot. The error bars represent the standard deviation of 5 independent experimental runs. **e**, Force–displacement curve for a stopper knot with H/D=6.6±0.1. The red-shaded region represents the standard deviation of 4 runs. The grey-shaded region represents the interval in the FEM data resulting from the range of the friction coefficients explored in the simulations (see legend); similarly for panel **f**. The points (i)–(vi) correspond to the configurations in Fig. 1. **f**, Normalized capsizing force, $F_0/(Mg)$, vs. H/D. The $\mu_{\mathrm{R-R}}$ and $\mu_{\mathrm{R-P}}$ values used in FEM are provided in the lower legends of panels **e** and **f**.

the knot undergoes capsizing, causing it to shift downward on the rod. We use the simulations to explore the impact of friction on capsizing systematically. We quantify the twist in a critical rod segment, revealing that the onset of capsizing is primarily due to friction-induced twisting between portions of the self-contacting rod. Additionally, we find that increasing the friction coefficient between the rod and the plate mitigates the onset of capsizing. Finally, we discuss the relevance of our findings to braided ropes.

2. Methods: Experiments

Our study focuses exclusively on the capsizing behavior of stopper knots, which involves geometric reconfigurations rather than other failure mechanisms, such as fracture. To this end, we introduce an experimental model system using composite rods that are nearly inextensible axially but elastic in bending and twisting, thereby excluding fracture and minimizing cross-sectional reduction during mechanical tests. This design yields structured rods that are transversely isotropic in their cross-sectional behavior, akin to braided ropes, as elaborated in Section 8, albeit with some differences that are also discussed there. The remainder of this section describes the protocols for the fabrication of the composite rods and for setting the initial knotted configuration. Finally, we present the mechanical testing procedure.

Fabrication of Composite Rods: Following a protocol introduced in Refs. [14,15], we fabricate rods via casting with vinyl polysiloxane (VPS, Elite Double 32, Zhermack; Young's modulus, E=1.25 MPa, Poisson's ratio, ν=0.5), with diameter D=8.3 mm and length L=35 cm. During casting, a thin Nitinol wire (NiTi, Dynalloy; D_{NiTi}=0.254 mm, E_{NiTi}=79.5 GPa, and ν_{NiTi}=0.33) is embedded at the centerline of the VPS rod. This wire is anchored at each rod end by an overhand knot against a circular, rigid Polyvinyl chloride (PVC) shim stock plate (thickness 0.75 mm) with a central hole; see Fig. 2**a**. The pronounced difference in axial stiffness between the VPS matrix and the wire core renders the composite rods essentially inextensible. While the end caps prevent global stretching, local sliding and debonding between the VPS and NiTi core are not excluded *a priori* and their absence remain subject to numerical validation. For reproducible frictional behavior, the rods were surface-treated with talcum powder (Milette, Migros), ensuring classic Amontons-Coulomb behavior with μ_{s}=0.41±0.04 and μ_{d}=0.35±0.02 for the static and dynamic friction coefficients, respectively, as detailed in § S1 of the S.I.

Preparation Protocol: To ensure reproducibility given the possible meta-stability induced by friction, we devised a two-step protocol for precisely setting the initial configuration of the system: (i) pre-tensioning of the knotted rod and (ii) applying a dead weight to its lower end. In the first step, we tied a loose figure-8 knot midway along the rod and aligned it vertically. The rod's upper end was threaded through the clearance hole (diameter d=10 mm$\gtrsim D$) of a horizontal acrylic *stopper plate* (thickness 10 mm; see Fig. 2**b**) and clamped to the load cell of a universal testing machine (UTM, Instron 5943). The lower surface of the plate was coated by a thin VPS film (thickness ≈0.5 mm), whose surface was also treated with talcum powder to ensure identical rod-plate and rod-rod frictional properties. The rod's lower extremity was subsequently clamped, and its end-to-end distance was increased using the UTM to set the rod pre-tension, P. In step (ii), the lower end was unclamped and, to keep the knot in place, attached to a dead load Mg (Fig. 2**b**) with M fixed at 0.2 kg and g denoting gravitational acceleration. Note that the weight of the dead load was chosen carefully to maintain the tightness and configuration of the knot nearly unchanged during the transition from step (i) to step (ii) of the protocol, from applying a pre-tension to freeing the lower end

of the rod. This precaution stabilized the response of the stopper knot during testing and enhanced the repeatability of the results. The initial configuration was characterized by the *knot size*, H, defined as the shortest distance between the outer edges of the knot; see Fig. 1**a**(i). The image processing analysis is detailed in § S2 of the S.I. We varied the pre-tension systematically within $1 \lesssim P/(Mg) \lesssim 3$, yielding different H values, as shown in Fig. 2**d**. The data evidence that H/D decreases with increasing $P/(Mg)$, as elaborated in Section 4.

Mechanical Testing: Following the protocol described above to set the initial configuration of a rod containing a figure-8 knot and a dead load on its lower extremity, the UTM was used to apply a pulling force on the rod's upper end. The experiments were conducted under imposed displacement at constant vertical velocity v=1 mm/s. Consequently, the knot was pushed against the stopper plate, which restrained its motion, thereby increasing the load in the system. During each mechanical test, we recorded the traction force, F, measured by the UTM as a function of the length of the displaced rod, δ. A representative force–displacement curve obtained from these experiments is plotted in Fig. 2**e** and will be discussed in Section 4.

3. Methods: Finite element simulations

In parallel to the physical experiments, we carried out numerical simulations using the finite element method (FEM, ABAQUS STANDARD 6.14-1, Simulia, Dassault Systems 2014). Upon validation, these simulations were particularly beneficial for exploring quantities that were not readily variable (*e.g.*, rod-rod and rod-plate friction coefficients) of accessible (*e.g.*, local rod twist during the capsizing mechanism) in the experiments. The FEM analysis employed a nonlinear dynamic-implicit scheme. An initially straight elastic rod was meshed with reduced hybrid 3D solid elements (`C3D8RH`). The mesh comprised 270 elements along the axial direction of the rod and 44 across the cross-section. The material was modeled as an incompressible neo-Hookean solid with Young's modulus E=1.25 MPa, consistently with the experiments. Two other values were also considered: E={0.52, 0.98} MPa.

To mimic the NiTi wire core of the experimental samples, a beam reinforcement was implemented at the centerline (see Fig. 2**c**), matching the geometric and material properties (D_{NiTi} and E_{NiTi}) in the experiments. Specifically, the Abaqus feature `stringer element` shared its nodes with the primary mesh. We also defined a node set along the axial direction, parameterized by arc length s, along the rod's outer surface. From the discrete coordinates $\boldsymbol{\xi}(s_i)$ along these outer nodes $i \in [1, 270]$, together with the nodes of the material centerline, $\boldsymbol{r}(s_i)$, we can define one of the directors orthogonal to the straight, undeformed centerline [1,16]:

$$\hat{\mathbf{d}}_1(s_i) \equiv \frac{\boldsymbol{\xi}(s_i) - \mathbf{r}(s_i)}{\|\boldsymbol{\xi}(s_i) - \mathbf{r}(s_i)\|}, \tag{1}$$

which facilitated the quantification of twist evolution between different loading states of the knot, as will be discussed in Section 7.

In both experiments and the simulations, the system experienced two types of frictional contact: self-contact between rod segments (denoted $R-R$ for '*Rod vs. Rod*') and contact between the rod and the stopper plate (denoted $R-P$ for '*Rod vs. Plate*'). Similar to previous studies [1,14,15,17], we modeled these contacts using the Amontons-Coulomb friction law, enforcing normal penalty forces combined with tangential frictional forces, implemented by a single friction coefficient. Proper assignment of this coefficient to the respective contact regions is crucial, a point that will be elaborated upon in Section 6.

Our knot-tying protocol for our axially reinforced composite rods is the same as that introduced for an elastic rod in Ref. [17], a recent study that also included experimental validation for a figure-8 knot. In the numerics, the initial configuration of the system was set identically to the experiments, tightening the figure-8 knot to a pre-tension, P, before releasing it to the dead load, Mg. Finally, the knot size, H, was determined as the shortest distance between the outer edges of the knot (Fig. 2**c**).

4. Characterization of the initial knot size

Prior to conducting the mechanical tests on figure-8 stopper knots (whose results will be presented in Section 5), it was essential to prepare the knotted samples via the protocol introduced in Section 2. This protocol was implemented in both experiments and simulations to ensure reproducibility, particularly given the potential of friction-induced metastability. The preparatory steps involved setting the pre-tension of the knotted rod and then applying a dead load at its lower extremity to establish the knot size, H. Fig. 2**b** and **c** show, respectively, representative snapshots from experiments and FEM of the prepared configurations before mechanical testing. This section focuses on characterizing these initial configurations as quantified by H.

In the inset of Fig. 2**d**, we plot the experimental and FEM (dimensional) data for H obtained after the preparation protocol versus the applied pre-tension, P, of the composite rod. Experimentally, the mass of the dead weight was fixed at M=200 g and E=1.25 MPa for the VPS matrix. In the FEM, two additional pairs of parameters were investigated, with (E=0.98 MPa, M=157 g) and (E=0.52 MPa, M=83 g). Under the hypothesis that H is set by the balance between the rod's bending stiffness ($E\pi D^4/64$) and the dead load (Mg), we construct the dimensionless group $\mathcal{K}=ED^2/(Mg)$. Note that the three pairs of parameters (E, Mg) were selected to yield a constant $\mathcal{K}$ = 44 (as explained in Section 2). In the *dimensionless* plot of Fig. 2**d**, with H/D versus $P/(Mg)$, we find a collapse of the data, confirming the physical similarity of the three systems and demonstrating that the rod's bending stiffness and the applied pre-tension are the primary ingredients dictating the knot shape. Additionally, this collapse demonstrates that embedding the stiff NiTi wire at the core of the elastomeric rod does not influence the scaling behavior of the elastic system, which deforms primarily through bending.

In Fig. 2**d**, the experiments (crosses) and the corresponding FEM data (circles) are in good agreement, serving as a first validation of the simulations. This agreement is particularly remarkable given the complex coupling between the underlying nonlinear geometry, elasticity, and frictional contact. Still, the FEM systematically under-predicts the experimental data. At this stage, we speculate that the reason for this offset may be due to our treatment of friction in the simulations. For the FEM data presented thus far, we prescribed both the rod-rod and rod-plate friction coefficients to μ = 0.33, the lowest dynamic friction coefficient measured experimentally, which is an over-simplification whose implications will be examined next.

5. Mechanical testing of the figure-8 stopper knots

Using the protocol described in Section 2, the figure-8 knot was loaded against the stopper plate. This section is dedicated to the results of these mechanical tests. We refer to the *pulled end* as the rod's upper extremity clamped to the UTM, and the *free end* is the lower extremity attached to the dead load. Below the pulled end, the rod traverses the clearance hole of the plate, with the knot situated below. Additionally, we denote the upper bent rod segment in contact with the plate as the *upper loop*, and the segment nearer to the free end as the *lower loop*.

In Fig. 1**a**, **b**, we displayed a series of experimental and FEM snapshots, labeled as (i)–(vi), exhibiting a single capsizing event, which is described next. At (i), the upper loop establishes contact with the plate, onto which it is then compressed; (i)–(ii). Once the upper loop makes full contact with the plate, the lower loop acts as a hook, lifting the free end; (ii)–(iii). The lower loop then opens the upper loop in a wedge-like manner; (iii)–(iv). Consequently, as quantified below, a friction-induced twist accumulates in the upper loop. The combined effect of the wedging and twisting causes the lower loop to overtake the upper one, with the latter rolling and snapping down towards the free end; (iv)–(v). Finally, in (vi), the figure-8 knot reaches a new traveled position closer to the free end. Continued pulling would result in recurrent capsizing events, each yielding progressively tighter

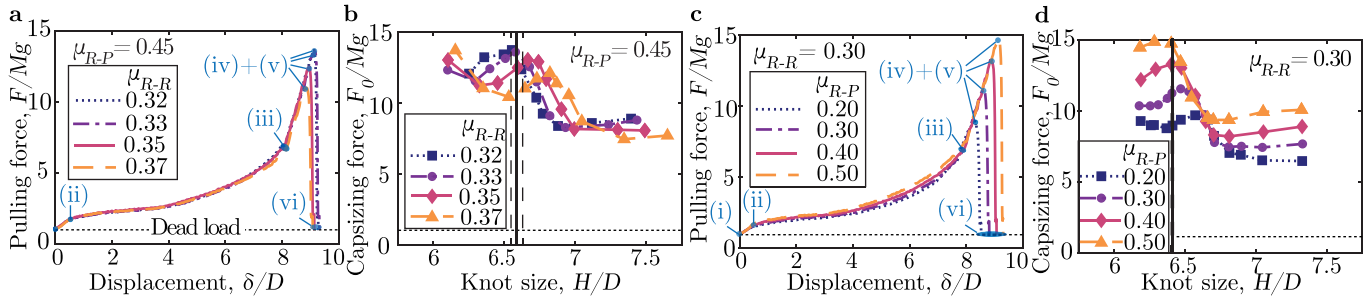

Fig. 3. Impact of friction on capsizing. **a** Normalized pulling force, $F/(Mg)$ vs. displacement, δ/D. **b** Capsizing force $F_0/(Mg)$ vs. knot size, H/D. In panels **a** and **b**, we fixed the rod-plate friction coefficient to $\mu_{\mathrm{R-P}}$=0.45 and varied the rod-rod friction coefficient, $\mu_{\mathrm{R-R}}$ (see legend). Panels **c** and **d** are analogous to **a** and **b**, respectively, but fixing $\mu_{\mathrm{R-R}}$=0.30 and varying $\mu_{\mathrm{R-P}}$ (see legend). In **a** (and **c**), the initial knot size is H/D=6.59±0.04 (and H/D=6.41±0.04), corresponding to the vertical lines in **b** (and **d**, respectively). In all panels, the horizontal dashed line represents the applied dead load, Mg, with M=0.2 Kg.

configurations. After several cycles, the knot would ultimately unravel through the free end. In the context of rock climbing (where the belay device would act as the stopper plate), this unraveling could be fatal as the rope would no longer provide the required tension for safety. The remainder of this study is dedicated to investigating the first capsize event.

In Fig. 2**e**, we present typical force–displacement curves for experiments and simulations for a knot of initial size H/D=6.6 ± 0.1 prepared with $P/(Mg)$=1.99 (the same as in Fig. 1). The normalized traction force, $F/(Mg)$, measured by the load cell, exhibits a monotonic yet nonlinear increase versus the normalized length of the displaced rod, δ/D. This force peaks at F_0, and, subsequently, drops close to zero. We define F_0 as the *capsizing force*: the maximum load-bearing capacity at capsizing. The labels (i)–(vi) correspond to those in Fig. 1, with the capsizing event occurring between (iv) and (v). Note that the nonlinearity of the force–displacement curves in Fig. 2**e** is not attributable to hyperelastic stretching; the NiTi wire at the centerline of the rod enforces near axial inextensibility.

Prior studies [1,14,17,18] have established that a *dynamic* friction coefficient is adequate for accurately capturing the self-contact interactions in a knotted rod. Thus, in our FEM simulations, we use the experimentally measured average and uncertainty of the dynamic friction coefficient ($\mu_{\mathrm{R-R}}$=0.35 ± 0.02) to characterize rod-rod-contact. For the rod-plate contact, we systematically explore the entire relevant range of friction coefficients, $\mu_{\mathrm{R-P}}\in$[0.33 0.45], spanning from the lowest dynamic to the highest static values. In Fig. 2**e**, we present FEM data for four force–displacement curves computed using the relevant limiting values, $\mu_{\mathrm{R-R}}$={0.33, 0.37} and $\mu_{\mathrm{R-P}}$={0.33, 0.45}. Overall, we find a good match between the experimental and FEM curves, and the (i)–(vi) events labeled in Fig. 1 occur at similar loading levels between the two. This agreement provides additional validation for the FEM simulations within the experimentally relevant range of the friction coefficients. These results evidence that the stopper knot system involves a complex interplay between static and dynamic frictional behavior.

In Fig. 2**f**, the experimentally measured, normalized capsizing force is plotted versus knot size, exhibiting a general decrease in $F_0/(Mg)$ with increasing H/D, albeit with some scatter (circles). In other words, a tighter initial configuration of the stopper knot yields a higher capsizing force. Concurrently, the FEM data in Fig. 2**f** were computed using the limiting friction coefficients discussed in the paragraph above (similarly to Fig. 2**e**). The envelope of these FEM data (shaded region) encompasses the experimental data, further validating the simulations. Each FEM curve exhibits an overall decreasing trend of $F_0/(Mg)$ with H/D, albeit non-monotonically; there is a 'bump' in each curve (at a characteristic knot size), whose location depends on the combination of $\mu_{\mathrm{R-R}}$ and $\mu_{\mathrm{R-P}}$. The mechanism behind this feature remains elusive, likely involving a complex interplay between geometry, contact pressure, and friction, and calls for a more in-depth future analysis.

6. Influence of friction on the capsizing mechanism

Having established the experimental validation of our FEM simulations, we now conduct systematic simulations to examine the influence of the frictional interactions (both rod-rod and rod-plate) on the capsizing of the figure-8 stopper knots.

First, we perform simulations with four values of the rod-rod friction coefficient, $\mu_{\mathrm{R-R}}$={0.32, 0.33, 0.35, 0.37}, while fixing the rod-plate friction coefficient at $\mu_{\mathrm{R-P}}$=0.45. In Fig. 3**a**, we plot the normalized force–displacement curves, $F/(Mg)$ vs. δ/D, for a stopper knot prepared with H/D=6.59±0.04. Interestingly, all four curves overlap between the loading levels (i) and (iv), irrespective of the values of $\mu_{\mathrm{R-R}}$ (the labels are the same as in Fig. 1). Nonetheless, for lower $\mu_{\mathrm{R-R}}$, the portion of the force–displacement curve beyond (iv) exhibits a more extended steep rise up to the onset of capsizing at (v), resulting in higher peak forces. In Fig. 3**b**, we plot the normalized peak force, $F_0/(Mg)$, as a function of H/D, for the aforementioned $\mu_{\mathrm{R-R}}$ values. All four cases exhibit the same qualitative behavior with a non-monotonic decrease of the capsizing forces. Specifically, higher capsizing forces are found for tighter figure-8 knots ($H/D\lesssim$6.5) and lower capsizing forces for looser configurations ($H/D\gtrsim$7). Note that increasing $\mu_{\mathrm{R-R}}$ also leads to a progressive shift of the curves toward higher values of H/D. In other words, reducing the rod-rod friction coefficient (while fixing that for rod-plate) requires a tighter initial knot configuration (with smaller H) to achieve comparable mechanical performance, as assessed by the capsizing force.

Next, we fix the rod-rod friction coefficient to $\mu_{\mathrm{R-R}}$=0.3, and systematically examine the influence of varying the rod-plate friction coefficient within the range $\mu_{\mathrm{R-P}}$={0.20, 0.30, 0.40, 0.50}. In Fig. 3**c**, we plot the corresponding force–displacement curves for the same knot size, H/D=6.41±0.04. Similarly to Fig. 3**a**, the curves overlap between (i) and (iv) but with a more extended final rise between (iv) and (v); the capsizing (peak) forces increase with $\mu_{\mathrm{R-P}}$. In Fig. 3**d**, we plot $F_0/(Mg)$ versus H/D for the four values of $\mu_{\mathrm{R-P}}$. All curves are characterized by a higher plateau for tighter configurations (small H/D) and a lower plateau for looser configurations (large H/D), with a transition between the two at $H/D\approx$6.5. There is a significant drop in the capsizing force across this transition. Consider, for instance, the figure-8 knot of size H/D=6.3. For $\mu_{\mathrm{R-P}}$=0.5, this stopper knot reaches $F_0\approx 15Mg$ but only $F_0\approx 9Mg$ for $\mu_{\mathrm{R-P}}$=0.2. Overall, the mechanical performance of the knots, as quantified by their capsizing force, increases with $\mu_{\mathrm{R-P}}$.

Combining the data in Figs. 3**b** and 3**d**, we conclude that increasing the rod-plate friction has a more important effect in enhancing the performance of the stopper knot than the rod-rod friction. These findings could serve as valuable guidelines for practical applications of performant stopper knots. We expect similar behavior for friction coefficients outside of the explored range, within reasonable experimental bounds for smooth elastic filaments, as long as Amontons-Coulomb friction law remains valid (see § S1 of the S.I.).

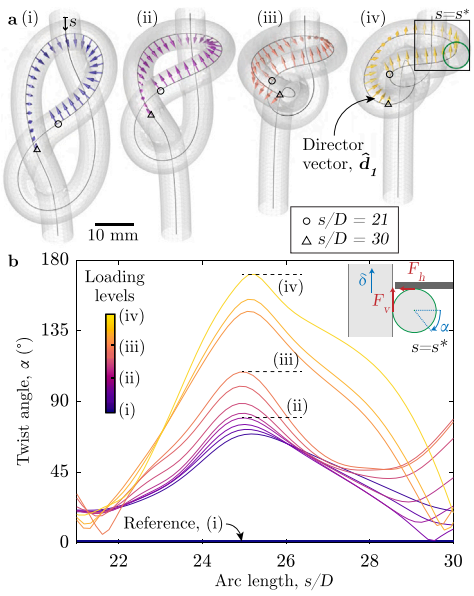

Fig. 4. Friction-induced twist in the upper loop. **a**, FEM-computed configurations at the loading levels, (i)–(iv) of Fig. 1, from the initial configuration (i) to the onset of capsizing (iv). Parameters: H/D=5.7 and μ_{R-R}=μ_{R-P}=0.33. The director vector, $\hat{\boldsymbol{d}}_1$, is represented in the upper loop, within $21 \leq s/D \leq 30$. **b**, Twist angle profiles, $\alpha(\tilde{s})$, computed using Eq. (2). Inset: Schematic of a cross-sectional rod cut at $s = s^*$; see (iv) in panel **a**.

7. Friction-induced twisting triggers capsizing

In this final section, we aim to elucidate the capsizing mechanism of figure-8 stopper knots, seeking to investigate the relation between F_0 and the frictional interactions at rod-rod and rod-plate contacts. Via FEM simulations, we will quantify the twisting in the upper loop of the stopper knot, analyzing the evolution of the director vector, $\hat{\boldsymbol{d}}_1(\tilde{s})$, as a function of normalized arc length, $\tilde{s}=S/D$, at various loading levels. Recall that $\hat{\boldsymbol{d}}_1(\tilde{s})$ was defined in Eq. (1) for the straight, unknotted rod.

In Fig. 4**a**, we present FEM-computed 3D visualizations of a stopper knot at the four loading levels preceding capsizing, (i)–(iv), corresponding to the labels in Fig. 1. The stopper plate is omitted for clarity. The rod centerline (thin solid line) is annotated with the $\hat{\boldsymbol{d}}_1(\tilde{s})$ director vector, only on the upper loop in the $21 \leq \tilde{s} \leq 30$ segment of the rod ($\tilde{s} = 0$ at the pulling end). To facilitate interpretation, we adopt the initial configuration in Fig. 4**a**(i) as the reference state, characterized by $\hat{\boldsymbol{d}}_{1,\mathrm{Ref}}(\tilde{s})$. For subsequent deformations, the upper-loop's twist angle is then computed with respect to this reference configuration as

$$\alpha(\tilde{s}) = \arccos\left(\frac{\hat{\boldsymbol{d}}_1(\tilde{s}) \cdot \hat{\boldsymbol{d}}_{1,\mathrm{Ref}}(\tilde{s})}{\|\hat{\boldsymbol{d}}_1(\tilde{s}) \cdot \hat{\boldsymbol{d}}_{1,\mathrm{Ref}}(\tilde{s})\|}\right). \tag{2}$$

In Fig. 4**b**, the $\alpha(\tilde{s})$ profiles are presented for varying loading levels (see adjacent color bar). By construction, $\alpha(\tilde{s})$=0 in the reference configuration (i). Upon loading, the twist-angle profiles become spatially heterogeneous (non-monotonic along $\tilde{s}$). As the loading increases from (i) to (iv), there is an overall increase of twist, particularly between stages (iii) and (iv). The twist angle remains substantially lower near the edges of the upper loop, at $\tilde{s}$={21, 30}, suggesting that the primary mechanism for twist accumulation in the upper loop is rod-rod friction caused by the vertical displacement (δ) of the rod.

The inset of Fig. 4**b** illustrates our interpretation of the capsizing mechanism. The schematic shows the cross-sectional cut highlighted in Fig. 4**a**(iv) at the point where a nearly horizontal segment of the rod at $s = s^*$ contacts an approximately vertical segment closer (in s) to the pulling end (where $s = 0$). The vertical displacement, δ, of the pulled rod activates a vertical friction force, F_v, on the adjacent rod segment with which it contacts. The build-up of the resulting twist, α, is constrained by the frictional interplay between the upper loop and the stopper plate, with a counteracting frictional force, F_h. Moreover, the higher capsizing forces for tighter knots reported in Figs. 2**f** and 3**b, d** can be attributed to the higher torsional stiffness of shorter upper-loop segments, L (torsional stiffness $\sim 1/L$), coupled with higher normal contact forces. This interpretive description of the capsizing mechanism is in accord with the results presented in Figs. 3 and 4.

8. Conclusions and discussion

In this study, we investigated the mechanics of capsizing in stopper knots. Delaying the onset of this phenomenon is important, as this class of knots is commonly employed to block a tensioned filament from passing through a constraining orifice. After carefully validating our FEM simulations with precision experiments, we systematically studied the effect of the frictional interactions on capsizing. We found that lower rod-rod friction coefficients can delay the onset of capsizing. Intriguingly, increasing the rod-plate friction has a far more important effect in enhancing the performance of the stopper knot than the rod-rod friction. To probe this behavior, we used the FEM simulations to quantify the local twist of the rod during the tightening process. We found that capsizing arises from the friction-induced torsional deformation of the rod segment in contact with the stopper plate. Furthermore, given that torsional stiffness is increased for shorter rod segments, tighter knots, whose upper loop has a shorter total arc length, capsize at higher loads.

Our experiments and FEM simulations were performed on composite elastic rods with a NiTi-wire core, ensuring near axial inextensibility while preserving elasticity in bending and twisting, as confirmed by the results in Fig. 2**d**. It is common to define the bending (B=EI) and torsional (C=GJ) stiffnesses of a rod, where E and G are the Young's and shear moduli, and I and J are the second and polar moments of area, respectively. In our elastic rods, these stiffnesses are intrinsically coupled as Γ=B/C=$(1+\nu)\approx 3/2$, since $\nu\approx 0.5$ for VPS. Establishing the relevance of our results on elastic rods to braided ropes, especially regarding the capsizing mechanism, onto which stopper knots are often tied in climbing and sailing for safety, remains an open problem. In §5.7 of Ref. [19], we have recently reported preliminary mechanical tests, in bending and torsion, of a set of braided ropes, finding that Γ<1 for these systems. This decoupling between B and C (with C>B) results in a higher torsional energy cost in braided ropes compared to bending, acting as an impediment to twisting deformation. Indeed, and in accord with the interpretation of the capsizing mechanism in Section 7, the higher energetic cost of torsion compared to bending significantly delays or may even inhibit the capsizing of common stopper knots tied in braided ropes.

We recognize that the comparative observations between elastic and braided filaments discussed above are mostly qualitative; a detailed quantitative comparison is premature since the two systems have different frictional properties, calling for a more systematic investigation. We hope that our findings will instigate future quantitative analysis of stopper knots in braided ropes, taking the elastic case we have studied in detail as a starting point.

CRediT authorship contribution statement

Paul Johanns: Conceptualization, Data curation, Formal analysis, Investigation, Methodology, Software, Validation, Visualization, Writing – original draft, Writing – review & editing, Funding acquisition. **Pedro M. Reis:** Conceptualization, Data curation, Funding acquisition, Investigation, Methodology, Project administration, Resources, Supervision, Visualization, Writing – original draft, Writing – review & editing.

Declaration of competing interest

The authors declare that they have no known competing financial interests or personal relationships that could have appeared to influence the work reported in this paper.

Data availability

Data will be made available on request.

Acknowledgments

This work was partially supported by the Fonds National de la Recherche, Luxembourg (12439430).

Appendix A. Supplementary data

Supplementary material related to this article can be found online at https://doi.org/10.1016/j.eml.2024.102134.

References

[1] T.G. Sano, P. Johanns, P. Grandgeorge, C. Baek, P.M. Reis, Exploring the inner workings of the clove hitch knot, Extreme Mech. Lett. 55 (2022) 101788, http://dx.doi.org/10.1016/j.eml.2022.101788.

[2] P. Batoux, A. Mallon, A. Gruyelle, M. Perche, Nœuds de jonction pour rappels, Technical Report, Ecole Nationale de Ski et d'Alpinism, 2021.

[3] T. Waitayawinyu, P.A. Martineau, S. Luria, D.P. Hanel, T.E. Trumble, Comparative biomechanic study of flexor tendon repair using FiberWire, J. Hand Surg. 33 (5) (2008) 701–708, http://dx.doi.org/10.1016/j.jhsa.2008.01.010.

[4] P. Johanns, C. Baek, P. Grandgeorge, S. Guerid, S.A. Chester, P.M. Reis, The strength of surgical knots involves a critical interplay between friction and elastoplasticity, Sci. Adv. 9 (23) (2023) http://dx.doi.org/10.1126/sciadv.adg8861.

[5] J.H. Maddocks, J.B. Keller, Ropes in equilibrium, SIAM J. Appl. Math. 47 (6) (1987) 1185–1200, http://dx.doi.org/10.1137/0147080.

[6] V.P. Patil, J.D. Sandt, M. Kolle, J. Dunkel, Topological mechanics of knots and tangles, Science 367 (6473) (2020) 71–75, http://dx.doi.org/10.1126/science.aaz0135.

[7] D. Tong, A. Choi, J. Joo, A. Borum, M. Jawed, Snap Buckling in Overhand Knots, J. Appl. Mech. 90 (4) (2023) 041008, http://dx.doi.org/10.1115/1.4056478.

[8] C.W. Ashley, The Ashley Book of Knots, Doubleday, New York, 1944.

[9] J.C. Turner, P.C. van de Griend, History and Science of Knots, World Scientific, 1996.

[10] N.C. Bloomsbury Publishing Plc, The Knot Bible: The Complete Guide To Knots and their Uses, Adlard Coles Nautical, 2013.

[11] P. Petit, Why Knot?, Abrams Image, 2013.

[12] C.C. Adams, The Knot Book: An Elementary Introduction to the Mathematical Theory of Knots, AMS Bookstore, Providence, RI, 2004.

[13] D. Tong, M. Khalil, M. Silva, G. Wang, B. Khoda, M. Jawed, Mechanical Response of Fisherman's Knots during Tightening, J. Appl. Mech. (2023) 1–11, http://dx.doi.org/10.1115/1.4063895.

[14] P. Grandgeorge, C. Baek, H. Singh, P. Johanns, T.G. Sano, A. Flynn, J.H. Maddocks, P.M. Reis, Mechanics of two filaments in tight orthogonal contact, Proc. Natl. Acad. Sci. USA 118 (15) (2021) http://dx.doi.org/10.1073/pnas.2021684118.

[15] P. Johanns, P. Grandgeorge, C. Baek, T.G. Sano, J.H. Maddocks, P.M. Reis, The shapes of physical trefoil knots, Extreme Mech. Lett. 43 (2021) 101172, http://dx.doi.org/10.1016/j.eml.2021.101172.

[16] B. Audoly, Y. Pomeau, Elasticity and Geometry, Oxford Univ. Press, 2010.

[17] C. Baek, P. Johanns, T.G. Sano, P. Grandgeorge, P.M. Reis, Finite element modeling of tight elastic knots, J. Appl. Mech. 88 (2) (2021) http://dx.doi.org/10.1115/1.4049023.

[18] P. Grandgeorge, T.G. Sano, P.M. Reis, An elastic rod in frictional contact with a rigid cylinder, J. Mech. Phys. Solids 164 (2022) 104885, http://dx.doi.org/10.1016/j.jmps.2022.104885.

[19] P. Johanns, Mechanics of Physical Knots: From Filaments in Contact to Surgical Suturing, EPFL, Lausanne, 2023, http://dx.doi.org/10.5075/EPFL-THESIS-9531.